1   Introducing LAB60: A 1/60° NEMO 3.6 numerical simulation of the Labrador Sea

2   Clark Pennelly[1*] and Paul G. Myers[1]

3   [1]1-26 Earth Sciences Building, University of Alberta, Edmonton, Alberta, Canada, T6G 2E3

4   *Correspondence to: Clark Pennelly (pennelly@ualberta.ca)

5

6   Abstract

7   A high-resolution coupled ocean-sea ice model is set up within the Labrador Sea. With a

8   horizontal resolution of 1/60°, this simulation is capable of resolving the multitude of eddies

9   which transport heat and freshwater into the interior of the Labrador Sea. These fluxes strongly

10   govern the overall stratification, deep convection, restratification, and production of Labrador

11   Sea Water. Nested domains within our regional configuration reduce computational costs,

12   allowing for a simulation that will span over 15 years up to near-present time. Three passive

13   tracers are also included: Greenland runoff, Labrador Sea Water produced during convection,

14   and Irminger Water which enters the Labrador Sea along Greenland. We describe the

15   configuration setup and compare against similarly forced lower-resolution simulations to better

16   describe how horizontal resolution impacts the Labrador Sea.

17

18   1.   Introduction

19   The Labrador Sea, between Canada and Greenland, plays a crucial role in the climate

20   system. Situated between the Canadian Arctic and the North Atlantic, multiple current systems

21   influence this deep basin. Cold and fresh Arctic water flows south through Fram Strait along

22   Greenland (de Steur et al., 2009), producing the East Greenland Current (EGC). The EGC flows to

23   the southern tip of Greenland, merging with warm and salty Irminger Water to become the

24   West Greenland Current (WGC) before flowing northwards along the western coast (Fratantoni

25   and Pickart, 2007). The WGC flows cyclonically around the Labrador Sea as well as into Baffin

26   Bay. Significant amounts of freshwater are supplied to this current system from both Davis

27   (Cuny et al., 2005; Curry et al., 2011; Curry et al., 2014) and Hudson Strait (Straneo and Saucier,

28   2008) as it travels around the Labrador Sea. The current system is called the Labrador Current

29   where it merges with the outflow from Hudson Strait (Lazier and Wright, 1993). The Labrador

30   Current travels southwards along the eastern coast of North America eventually leaving the

31   Labrador Sea.

32   Numerous eddies are generated throughout the Labrador Sea, both from high lateral

33   density gradients which exist during the convection season (Frajka-Williams et al., 2014) as well

34   as from baroclinic and barotropic instabilities that occur within the boundary currents (Chanut

35   et al., 2008; Gelderloos et al., 2011). The continental slope along the west coast of Greenland

36   has a pronounced change in topography that induces instability of the current system,

37   generating eddies (de Jong et al., 2016). These eddies, known as Irminger Rings, contain a

38   significant amount of freshwater at the surface as well as subsurface heat. Irminger Rings (15-

39   30km radius) typically travel southwestwards into the interior of the Labrador Sea and have a

40   lifespan of up to two years (Lilly et al., 2003). Eddies generated along the Labrador Coast also

41   contain a significant amount of freshwater (Schmidt and Send, 2007; McGeehan and

42   Maslowski, 2011; Pennelly et al., 2019). Regardless of where they are produced, these

43   boundary current eddies often export their properties towards the centre of the basin (Pennelly

44   et al., 2019), influencing the deep convection which occurs. Convective eddies are generated

45   from baroclinic instability which arises from large horizontal density gradients during the

46   convective season (Marshall and Schott, 1999). Convective eddies are much smaller with a

47   radius between 5 and 18 km (Lilly et al., 2003). These eddies are less studied than the other

48   eddy types, partly due to a lack of observations (Lilly et al., 2003) as well as their small size

49   which requires high-resolution models to adequately resolve. Research into the role of each of

50   the above eddies and their role in restratifying the Labrador Sea is still ongoing; there is no

51   consensus on which eddy may be more important, though many have narrowed it down to

52   Irminger Rings and convective eddies (Chanut et al., 2008; Gelderloos et al., 2011; Rieck et al.,

53   2019).

54   Deep convection is a rather rare occurrence, only known to occur at a few places in the

55   ocean. The reason so few places exist is the stringent criteria to produce deep convection: weak

56   stratification that can be enhanced via isopycnal doming as a result of cyclonic circulation, and

57   intense air-sea buoyancy loss (Lab Sea Group, 1998; Marshall and Schott, 1999). Cyclonic

58   circulation and the lateral input of salty Irminger Water helps keep the Labrador Sea weakly

59   stratified. Furthermore, the Labrador Sea experiences strong heat loss during the winter period

60   due to the very cold mid-latitude cyclones which frequent the region (Schulze et al., 2016). The

61   overlying cold and dry air forces a significant flux of heat from the ocean to the atmosphere.

62   This loss of heat promotes the surface layer to increase in density, overturning the weakly

63   stratified water column such that the mixed layer can exceed 2000m in depth (Yashayaev,

64   2007), producing a thick uniform water mass known as Labrador Sea Water (LSW).

65   Once the convective winter ends, the Labrador Sea quickly restratifies itself within 2-3

66   months (Lilly et al., 1999), primarily due to large horizontal density gradients that form

67   convective eddies (Lilly et al., 2003; Rieck et al., 2019) as a result of the deep convection period

68   (Frajka-Williams et al., 2014). The boundary currents continuously shed eddies with relatively

69   buoyant water towards the interior Labrador Sea (Straneo, 2006), increasing stratification. This

70   occurs along the west Greenland and Labrador coasts, though research suggests that the

71   former supplies more freshwater (Myers, 2005; Schmidt and Send, 2007; McGeehan and

72   Maslowski, 2011; Pennelly et al., 2019).

73   LSW is exported out of the Labrador Sea primarily by the Deep Western Boundary

74   Current (Kieke et al., 2009), though it also spreads eastwards at a slower rate. While LSW is the

75   lightest component within the Deep Western Boundary Current, it is one of the water masses

76   which make up the lower limb of the Atlantic Meridional Overturning Circulation (AMOC). As

77   the overturning circulation transports a significant amount of heat and dissolved gasses

78   between the equator and polar regions, changes in the production of deepwater can influence

79   the overturning circulation and ultimately the climate (Bryden et al., 2005). With polar

80   amplification driven by the positive ice-albedo feedback loop, additional freshwater from

81   melted ice enters the EGC and WGC (Bamber et al., 2012). The Labrador Sea is experiencing an

82   increase in freshwater that can be capable of capping convection and preventing LSW from

83   being formed, ultimately reducing the AMOC strength (Böning et al., 2016). However, a non-

84   local increase in the surface freshwater flux may promote AMOC strengthening (Cael and

85   Jansen, 2020) or compensate the local effects of additional freshwater (Latif et al., 2000). Long

86   climate simulations allow investigation into any AMOC regime shifts that shorter, higher-

87   resolution simulations may miss. With such different conclusions, freshwater's influence on the

88   AMOC is not fully known and may vary at different convection regions.

89   While satellite altimetry provides a wealth of information including sea surface height

90   anomalies, geostrophic currents, and waves, hydrographic cruises within the Labrador Sea are

91   often limited to the restratification period when the Labrador Sea is more hospitable for

92   scientific operations. Argo floats, autonomous drifting profilers which can sample down to

93   2000m, have become a popular instrument to acquire in-situ data. However, they still lack

94   coverage within the Labrador Sea which can experience deep convection below their sampling

95   depth (Yashayaev, 2007). Numerical modelling is a useful tool to explore this data-sparse

96   region, though it has its limits. Simulations within the Labrador Sea often experience a drift in

97   model data, producing a Labrador Sea which slowly increases in salinity, and thus density

98   (Treguier et al., 2005; Rattan et al., 2010). Coarse-resolution simulations suffer even further,

99   often overproducing the spatial area of deep convection (Courtois et al., 2017), primarily as a

100   result of not resolving important small-scale features including eddies. These eddies supply the

101   Labrador Sea with significant heat (Gelderloos et al., 2011) and freshwater fluxes (Hátún et al.,

102   2007), both strongly impact the stratification, convection, and production of deep water.

103   Increased horizontal resolution helps produce these eddies and their important fluxes into the

104   interior of the Labrador Sea but numerical drift still is present within high-resolution

105   simulations, albeit reduced in severity (Marzocchi et al., 2015).

106   Numerous high-resolution simulations have been carried out within the North Atlantic.

107   VIKING20X (Rieck et al., 2019), and its predecessor VIKING20, are global 1/4° simulations which

108   have a high-resolution 1/20° nest. VIKING20X is a multi-decade simulation which is capable of

109   resolving eddies within the Labrador Sea. However, simulations with 1/20° horizontal resolution

110   may not resolve sub-mesoscale processes (Su et al., 2018) that can impact stratification by

111   carrying heat and freshwater; higher-resolution is needed. The 1/50° HYCOM (Chassignet and

112   Xu, 2017), 1/60° NATL60 (Fresnay et al., 2018) and eNATL60 (Le Sommer et al., in prep) provide

113   great insights on the importance of resolving eddies. However, computational expense with

114   such high-resolution simulations is very high, both in computer time and operational costs. This

115   often forces higher-resolution simulations to have a reduced length, perhaps only a few years.

116 The Labrador Sea experiences significant interannual variability (Fischer et al., 2010) and such

117 short simulations may completely miss any connection between LSW production and changes

118 in the AMOC. As such, any high-resolution simulation which is capable of resolving the fine

119 scale features within the Labrador Sea should be carried out for many years to further

120 understand the climate system. Resolving the full North Atlantic at high resolution (1/60°) and

121 carrying out a simulation for longer than 10 years would currently be extremely expensive; the

122 above 1/60° simulations are 5 or so years in length. However, one can incorporate nested

123 domains to increase horizontal resolution with a relatively minor increase in computing cost.

124   To simulate the Labrador Sea as accurately as possible, we set up a complex numerical

125 configuration which achieves very high resolution within the Labrador Sea while keeping

126 computing costs low such that we will produce over 15 years of simulated data. This simulation

127 will be kept up to near-present time, lagged a few months depending on the availability of

128 forcing data. The high resolution allows for explicit representation of eddies which are crucial to

129 controlling the stratification within the region. We will first describe the model configuration in

130 detail and then compare against similarly-forced lower-resolution simulations to understand

131 how changes in horizontal resolution impacts model results in the Labrador Sea.

132

133   2. Methods

134   The numerical model used for our high-resolution simulation is the Nucleus for

135 European Modelling of the Ocean (NEMO; Madec, 2008), version 3.6, which is coupled to a sea-

136 ice model, LIM2 (Fichefet and Maqueda, 1997). The 1/4° Arctic Northern Hemisphere Atlantic

137 configuration (ANHA4; Fig 1a) is used and includes a double nest via the Adaptive Grid

138 Refinement in FORTRAN package (AGRIF; Debreu et al., 2008). The AGRIF software allows for

139 high-resolution nests to communicate along their boundaries, passing information back and

140 forth between domains. The parent ANHA4 domain extends from Bering Strait, though the

141 Arctic and North Atlantic, to 20°S in the South Atlantic. The parent domain's nest uses a spatial

142 and temporal refinement factor of three, bringing resolution to 1/12° and the time step to 240s

143 (Table 1) in the North Atlantic Sub Polar Gyre domain (SPG12; Fig 1b). An ANHA4 configuration

144 with a SPG12 nest has been evaluated before by investigating how model resolution influences

145 Labrador Sea Water formation (Garcia-Quintana et al., 2019) as well as eddy formation and

146 eddy fluxes in the North Atlantic Current (Müller et al., 2017; Müller et al., 2019). Another nest

147 is implemented within the SPG12 domain, using a spatial and temporal refinement of five,

148 increasing the horizontal resolution from 1/12° to 1/60° and reducing the time step to 48s

149 within the Labrador Sea (LAB60; Fig 1c). All nests allow two-way communication such that the

150 parent domain supplies boundary conditions while the daughter domain returns interpolated

151 values to all associated parent grid points. All domains have different horizontal grid spacing

152 but they share the same vertical grid which is set to 75 geopotential levels (Fig. 1d) using partial

153 steps (Barnier et al., 2006). This simulation involves three domains (ANHA4, SPG12, and LAB60)

154 although we primarily discuss what occurs within the 1/60° nest.

155   A total variance dissipation scheme (Zalesak, 1979) was used in all domains to calculate

156 horizontal advection. A Laplacian operator was used to compute lateral diffusion in all domains,

157 while a bi-laplacian operator was used for lateral momentum mixing. As some model

158 parameters are grid-scale dependent, Table 1 displays these settings. As lateral boundary

159 conditions have been shown to be very important at producing Irminger Rings in high-

160 resolution simulations (Rieck et al. 2019), we used no-slip lateral boundary conditions within

161 the LAB60 domain while the other domains had free-slip conditions. Model mixed layer depths

162 were calculated via the vertical gradient in temperature and salinity (Holte and Talley, 2009) as

163 opposed to a 0.01 kg m^{-3} change in potential density between the surface and the bottom of

164 the mixed layer; the latter method can produce deeper mixed layers than observations suggest

165 (Courtois et al., 2017). Settings not listed in Table 1 indicate that all domains have an identical

166 value or option; some of these important settings are shown in Table 2.

167   Model bathymetry was interpolated from the 1/60° ETOPO GEBCO dataset (Amante and

168 Eakins, 2009) to each domain's grid with bathymetric smoothing along nest boundaries was

169 carried out in order to conserve volume where the parent domain supplies boundary conditions

170 to the daughter domain. All domains were initialized from GLORYS1v1 (Ferry et al., 2009), a

171 global reanalysis ocean simulation, at the beginning of 2002. Monthly open boundary

172 conditions (3D T, S, U, V, and 2D SSH and ice values) across Bering Strait and 20° S were

173 supplied to the ANHA4 domain. These boundary conditions were linearly interpolated from

174   monthly values, overriding the values within the boundary without the use of a sponge layer.

175   Runoff was supplied via Dai et al. (2009) while we also included Greenland runoff as estimated

176   from a surface mass-balance model (Bamber et al., 2012). Without an iceberg model

177   functioning with the AGRIF software, we treated all solid runoff as a liquid, thus capturing the

178   full freshwater mass at the cost of accuracy in the spatial and temporal placement of

179   freshwater emitted from icebergs.

180   Precipitation, shortwave radiation, downward longwave radiation, 2 meter specific

181   humidity, 2 meter temperature, 10 meter meridional and 10 meter zonal winds originally were

182   supplied from the Canadian Meteorological Centre's Global Deterministic Prediction System's

183   Reforecast product (CGRF; Smith et al., 2014). While high in temporal (hourly) and spatial

184   resolution (33 km in the Labrador Sea), we found the air-sea fluxes were slightly too weak to

185   sustain deep convection after 2010. Rather than start completely over, we switched the

186   atmospheric forcing in 2007 (Fig. 2) when LAB60's mixed layer was still similar to observations.

187   Starting on 1 Jan 2007, we used the DRAKKAR Forcing Set 5.2 (DFS; Dussin et al., 2016). DFS

188   supplies data at 3 hour increments for wind, temperature, and humidity, while precipitation

189   and radiation are daily. DFS has a spatial resolution which is approximately 45 km within the

190   Labrador Sea. Our own analysis of the CGRF data showed a 2002-2015 average yearly heat loss

191   of 47 W m^{-2} from the interior Labrador Sea while DFS removed 53 W m^{-2} (Pennelly and Myers,

192   submitted). Increasing the horizontal resolution likely increased the horizontal buoyancy fluxes

193   and rendered the CGRF's air-sea heat loss, which was appropriate in our ANHA4 and ANHA12

194   configuration, inadequate. The decision to swap to DFS was based on its greater heat loss,

195   promoting a better mixed layer depth throughout the Labrador Sea, though a different forcing

196   product will eventually be needed as DFS does not currently extend past 2017. Supplemental

197   Fig. 1 depicts the difference in mixed layer depth between the LAB60 simulation forced by

198   CGRF, when forced with CGRF through 2007 and then forced by DFS, as well as what ARGO

199   observations suggest. The weaker air-sea heat loss as forced by the CGRF product leaves the

200   mixed layer with little interannual variability that doesn't compare well with observations.

201   Early testing showed that adding passive tracers increases the computing resources

202   required by about 20% per passive tracer. To keep the simulation from requiring too many

203   resources, we limited LAB60 to three passive tracers:

204   1. Liquid runoff from Greenland

205   2. Irminger Water (T> 3.5°C, S>34.88) which flows westward past Cape Farwell (Fig. 3b)

206   3. Labrador Sea Water (σ_θ>27.68 kg m^{-3}) formed within the mixed layer of the Labrador

207   Sea (Fig. 3c)

208   Runoff from Greenland was included due to the importance of Greenland's freshwater

209   contribution to changes within the Labrador Sea. Water mass definitions for Irminger Water

210   and Labrador Sea Water were selected based on previous studies (i.e. Kieke et al., 2006; Myers

211   et al., 2007). Note that there is no maximum density criteria given to our Labrador Sea Water

212   tracer- the tracer is formed throughout the water column until it reaches the bottom of the

213   mixed layer. Figure 3 illustrates both the source regions as well as the tracer extent as of 1 Jan

214   2010. While these water masses have been studied before (Kieke et al., 2006; Myers et al.,

215   2007; Böning et al., 2016), there has been no attempt to use them as passive tracers at a

216   resolution higher than 1/20° (Böning et al., 2016).

217   The LAB60 simulation originally started on the Graham cluster of Compute Canada.

218   Other high-resolution simulations often use thousands of computer processors but our

219   simulation could not run on more than 672 CPUs on this cluster as it would stall during domain

220   construction. The years 2002-2007 were carried out on Graham, after which a new allocation

221   on a different high performance Compute Canada cluster, Niagara, became available to us. The

222   LAB60 simulation on Niagara did not suffer from the same issue as it did on Graham and we

223   were able to use many more processors. Initial testing found a substantial increase in the

224   number of days simulated per job submission when the number of CPUs was increased from

225   672 to 3000; tests using 4000 CPUs showed no further improvement. Thus, we carried out the

226   remainder of the LAB60 simulation with 3000 CPUs. Each job submission required around 22

227   hours to carry out, providing 40 days of model output. The real time to finish each 40 day

228   submission naturally varied across the year, increasing during winter which we attribute to the

229   sea-ice model.

230   A spin-up period (Fig. 2) was required as the model quickly went unstable and crashed.

231   We attribute this to the interpolation of the 1/12° GLORYS1v1 data onto the LAB60 grid; the

232   resulting data were not smooth enough and numerical noise was generated, leading to model

233   failure. To reduce this noise, a gradual spin-up procedure took place. First, we kept the

234   numerical timestep very low (2s in LAB60) when the model was initialized. We also set the

235   1/60° nests' eddy viscosity and diffusivity values to be equal to those within the SPG12 nest.

236   We gradually increased the timestep and reduced the viscosity and diffusivity values over the

237   first year (2002) to what is within Table 1. Other than also increasing the timestep to stay in line

238   with LAB60, no other values were changed across the coarser ANHA4 and SPG12 domains. To

239   allow LAB60 to adjust to the final settings, we consider the 2003 year to be an adjustment year

240   (Fig. 2).

241   To assess the validity of LAB60, model results were compared against AVISO satellite

242   data (https://www.aviso.altimetry.fr/), specifically U/V geostrophic velocities which are derived

243   from the sea surface height. Argo profiler data (http://www.argo.net/) was also used to assess

244   the mixed layer. Bottle data from cruise 18HUD20080520, accessed from CCHDO

245   (https://cchdo.ucsd.edu/cruise/18HU20080520) on 10 April 2018 was used to compare

246   observations across the AR7W section.

247

248   3. Model Simulation Results

249   To understand what is gained by resolving the Labrador Sea at 1/60°, we compare the

250   output of our LAB60 simulation with similarly forced ANHA simulations at both 1/4° (ANHA4)

251   and 1/12° (ANHA12). The large-scale circulation (top 50m) is shown for our 3 simulations (Fig. 4)

252   as well as AVISO geostrophic velocities. All simulations have greater speed within the West

253   Greenland Current (ANHA4: up to 0.8; ANHA12: 0.8; LAB60: 0.6; AVISO: 0.4 m s^{-1}) and Labrador

254   Current (ANHA4: up to 0.6; ANHA12: 0.6; LAB60: 0.4; AVISO: 0.4 m s^{-1}) as altimetry observations

255   suggest slower speeds here. However, Lin et al., (2018) found maximum speed up to 0.74 m s^{-1}

256   along the west coast of Greenland. Both the ANHA4 and ANHA12 configuration have larger

257   values further up the western coast of Greenland, as well as connecting the West Greenland

258   Current and the Labrador Current; features that do not occur in both LAB60 and observations.

259   As LAB60 and observations have less average speed occurring within these boundary currents,

260   we suspect that all configurations have some large differences in eddy activity, particularly

261   where these boundary currents are.

262   Eddy kinetic energy (EKE: $0.5(\overline{U_g'^2} + \overline{V_g'^2})$, Fig. 5) was calculated from geostrophic

263   velocity anomaly based on the sea level anomaly (SLA) from the 2004-2013 mean state:

$$U_g' = -\frac{g}{f}\frac{SLA}{\Delta y}$$

$$V_g' = -\frac{g}{f}\frac{SLA}{\Delta x}$$

264   where g is the gravitational constant, f is the Coriolis parameter, and Δy and Δx are model grid

265   length. Overbars indicate the 2004-2013 mean value while primed variables indicate a deviation

266   from the mean state. AVISO observations were already supplied as geostrophic velocities.

267   High levels of EKE can be found along the west coast of Greenland (Fig. 5), extending into the

268   interior of the basin around 62° N, as well as along the Labrador coast's shelf break. The path

269   extending from the west coast of Greenland is mostly due to Irminger Rings which leave this

270   coast and travel westward (Chanut et al., 2008). While the EKE extending from west Greenland

271   enters the interior of the Labrador Sea, that which stems from the Labrador coast does not

272   penetrate far into the interior. The ANHA4 simulation has low EKE along the west coast of

273   Greenland (around 100 $cm^2 s^{-2}$) and along the Labrador Coast's shelf break (10-30 $cm^2 s^{-2}$). The

274   ANHA12 simulation shows improvement, having much higher EKE extending from west

275   Greenland (100-300 $cm^2 s^{-2}$) however the EKE does not quite extend into the interior of the

276   Labrador Sea but instead remains in the northern Labrador Sea. Furthermore, there is

277   additional EKE along the Labrador shelf break (30-50 $cm^2 s^{-2}$) compared against ANHA4. The

278   LAB60 simulation shows further improvement as the EKE signature from the west Greenland

279   coast is greater (100-1000 $cm^2 s^{-2}$) and now enters into the interior of the Labrador Sea. A

280   notable increase in EKE also occurs along the Labrador shelf break (100-200 $cm^2 s^{-2}$) and within

281   the interior Labrador Sea (10-100 $cm^2 s^{-2}$). LAB60 matches well against observations along the

282   west coast of Greenland and the Labrador shelf break (both above 1000 $cm^2 s^{-2}$) as well as the

283   interior Labrador Sea (10-100 $cm^2 s^{-2}$). LS60's higher interior EKE may be partially from

284   convective eddies that are formed during the wintertime. However, LAB60 has lower EKE within

285   the Northwest Corner where ANHA4, ANHA12, and the observations exceed 1000 cm^2 s^{-2} over a

286   wide area. LAB60 matches the spatial distribution albeit with reduced EKE.

287   The differences in the EKE field between these configurations identify that each

288   simulation is resolving features of varying spatial scales. The ANHA4 simulation, with low EKE

289   within the Labrador Sea, does not adequately resolve eddies in this region, as illustrated with a

290   snapshot of normalized model relative vorticity (Fig. 6). However, the larger scale meanders

291   within the North Atlantic Current are visible. ANHA12 shows a greater degree of mesoscale

292   features (50 to 500 km), though distinct eddies within the Labrador Sea are also not resolved.

293   LAB60 resolves eddies along both the west coast of Greenland as well as the Labrador Coast. A

294   video showing LAB60's normalized relative vorticity is shown in Supplementary Video 1.

295   A few Irminger Rings are shown in Fig. 7, a snapshot in time from 26 July 2007. A newly

296   spawned ring (Fig. 7c) shows very strong surface speeds (up 0.6 m s^{-1} for Ring A; Fig. 7a) while

297   older eddies to the south have reduced speeds (up to 0.3 m s^{-1} for Ring B; Fig. 7a). To

298   investigate the stratification strength, we calculate the amount of energy needed to produce a

299   neutrally stratified column extending down to some reference depth, *h*. This proxy, called

300   convective energy, is given by:

$$Convective\ energy(h) = \frac{g}{Area} \int \int \left[h\,\rho_\theta(h) - \int_0^h \rho_\theta(z)\,dz \right] dA$$

301   where *g* is the gravitational constant, *Area* is the total surface area over our region of interest

302   (Fig. 1c), *h* is the reference depth (2000m used in this study), ρ_θ *(z)* and ρ_θ *(h)* are the potential

303   density at each grid cell and the potential density of the grid cell at the reference depth, and *A*

304   is the surface area of each grid cell. A strongly stratified column of water corresponds to a high

305   convective energy value. A snapshot of convective energy (Fig. 7b) shows that most of these

306   eddies have substantially higher amounts compared to the background Labrador Sea,

307   suggesting that the cool and fresh WGC water, as well as warm and salty Irminger Water keep

308   these eddies strongly stratified. However, these eddies age within the Labrador Sea, and while

309   a new eddy has strong stratification (>3000 J m^{-3}), an eddy which has evolved over many

310   months (Fig. 7d) has weaker stratification (about 2000 J m^{-3}). Older eddies may have very weak

311   stratification as they may have experienced two convective winter periods of buoyancy

312   removal. This has been noted before, as Lilly et al. (2003) found aged Irminger Rings with a

313   mixed layer that surpassed 1000m.

314   These differences in resolving the mesoscale (50 to 500 km) and sub-mesoscale (<50

315   km) processes within each simulation produced significant changes within the Labrador Sea as

316   seen from modeled convective energy values as averaged from 2004-2013 (Fig. 8). Resolving

317   few eddies, the ANHA4 simulation's interior Labrador Sea lacks the buoyancy flux and remains

318   very weakly stratified across a wide region. The ANHA12 simulation partially resolves some

319   mesoscale features and eddy fluxes from the Greenland coast which supplies buoyancy to the

320   Northern Labrador Sea and has higher convective energy. Furthermore, the spatial extent of

321   the weakly stratified region has shrunk and resides primarily within the Labrador Sea, as

322   opposed to ANHA4 which spills out of the basin. LAB60, fully capable of resolving buoyant

323   eddies from the Greenland and Labrador coast, as well as convective eddies, has a much

324   stronger degree of stratification in the interior region. A visible path of strong stratification

325   appears around 60°N along this coastline, eventually extending away from the coastline around

326   62°N. This path is consistent with the general path that simulated Irminger Rings take (Chanut

327   et al., 2008). Supplemental Video 2 shows the convective energy of the LAB60 simulation from

328   2004 through the end of 2013.

329   The ANHA4 simulation experiences weaker stratification in the Labrador Sea than

330   ANHA12 and LAB60, driving a deeper maximum mixed layer that also covers a larger spatial

331   extent (Fig. 9). However, the maximum mixed layer depth as simulated by ANHA4 and ANHA12

332   greatly exceed what Argo observations suggest (Fig. 9d). ANHA12 has higher EKE within the

333   WGC, supplying more buoyancy to the northern portion of the Labrador Sea, reducing both the

334   vertical extent of the mixed layer as well as the spatial extent where the mixed layer is deeper

335   than 1000m. LAB60 has higher EKE than ANHA12, and the vertical and spatial extent of deep

336   mixing is reduced even further. LAB60's mixed layer is far more similar to what ARGO

337   observations suggest, suggesting the additional eddy fluxes to be fairly accurate. The evolution

338   of LAB60's mixed layer depth is shown in supplemental video 3 from 2004 through the end of

339   2013.

340   After the bottom of the mixed layer returns to the near-surface, a newly formed LSW

341 mass is left behind. To account for density drift, we allow the LSW classification to evolve in

342 time, unlike our LSW passive tracer. We calculated LSW density and thickness by binning by

343 potential density, referenced to 1000 dbar, with bin lengths of 0.001 kg m^{-3}. This was carried

344 out within the black outlined polygon in Fig 1c for each daily output file per year. The density

345 bin which had the thickest layer across the year was set as the maximum density of LSW for

346 that year. The minimum density was defined to be 0.02 kg m^{-3} less than the maximum density.

347 Linear interpolation occurred between years to allow for a gradual shift in density to prevent

348 staircase patterns from emerging. Large differences in both the density as well as the thickness

349 are present between the simulations shown in Fig. 10. The ANHA4 and ANHA12 simulations

350 have similar density values of LSW while the LAB60 simulation is less dense. While the

351 interannual variability matches fairly well across all configurations, the density values suggested

352 by LAB60 match far closer to ARGO observations (32.34 to 32.36 kg m^{-3}; Yashayaev and Loder,

353 2016) during the same time period. We suspect the denser LSW formed by ANHA4 and ANHA12

354 is primarily attributed to the lack of buoyancy coming from Greenland. As similar air-sea heat

355 losses should occur in all three configurations, the weaker stratification of ANHA4 and ANHA12

356 indicates that deep mixing is more likely producing not only a denser LSW layer, but also a

357 thicker one. Yashayaev and Loder (2016) also investigated the thickness of LSW (their Fig. 8),

358 and while our simulations do not quite capture the same interannual variability and amplitude

359 suggested their analysis using ARGO profilers, LAB60 is far more accurate than the lower-

360 resolution configurations.

361   All simulations encounter some degree of numerical drift within the Labrador Sea (Fig.

362 11), judging from the salt and heat content change as calculated between the surface and

363 seafloor within the polygon in Figure 1 since 2004. ANHA4 experiences the most drift in both

364 salt and heat, helping us understand why LSW is so dense in this simulation. ANHA12 also

365 experiences drift, though slightly less severe. LAB60 has a small but gradual increase in both salt

366 and heat content although it is difficult to state if this is drift or simply interannual to decadal

367 variability. Regardless of the cause, LAB60's change in both heat and salt content is very

368 minimal compared against the lower-resolution simulations.

369   When compared against observations across the Atlantic Repeat Hydrography Line 7

370   West (AR7W; Fig 12), LAB60 is slightly warmer (about 0.25 °C) and saltier (about 0.05 kg m^{-3})

371   throughout the interior. This causes LAB60 to be slightly denser with isopycnals residing higher

372   than observations during this cruise suggest. Observations were not carried out above

373   Greenland's continental slope, although they show some presence of the warm core of the

374   WGC which the model captures. Salinity values close to the Labrador coast compare well while

375   LAB60 is slightly warmer (about 0.5 °C) above the continental shelf.

376   The three passive tracers implemented within the full LAB60 configuration (Fig. 3) show

377   where Greenland runoff, Irminger Water, and Labrador Sea Water travel to. These tracers were

378   selected because they either contain a significant amount of buoyant water compared to the

379   Labrador Sea, or are produced via convection in the Labrador Sea. From this image on 1 Jan

380   2010, we see a large portion of Greenland's runoff (Fig. 3a) resides within Baffin Bay as well as

381   along the Labrador Coast. Some of this tracer is present where the ocean depth is greater than

382   2000m. A few Irminger Rings are identifiable, due to their thicker freshwater cap, which are in

383   water deeper than 3000m. Little exchange appears to occur along the Labrador Current until

384   the vicinity of Flemish Cap, after which a significant portion of the tracer propagates eastward.

385   Supplemental Video 4 shows this the evolution of this tracer from 2004 through the end of

386   2013.

387   Irminger Water (T>3.5°C, S> 34.88; Fig. 3b) which flows west past Cape Farwell, enters

388   the interior Labrador Sea with the greatest amounts where the seafloor is at a depth between

389   2000 and 3000m. Similar as above, individual Irminger Rings are visible, containing a larger

390   amount of Irminger Water than the surrounding water. This water mass also flows along the

391   Labrador Coast until it is in the vicinity of Flemish Cap. Supplemental Video 5 shows this the

392   evolution of this tracer from 2004 through the end of 2013.

393   Our Labrador Sea Water tracer (Fig. 3c) is traced where the mixed layer produces water

394   with a potential density above 1027.68 kg m^{-3} within the black contour identified in the figure.

395   This definition differs compared to our method of classifying LSW as we did not implement any

396   FORTRAN code to detect and compensate for density drift of our simulation, instead sticking to

397   a strict density classification for this tracer. As this image was made at the start of the

398   convection season, the current deep patch is a freshly produced layer that reaches up to 800m

399   deep. After forming, LSW spreads southwards along the Labrador shelf break as well as to the

400   southeast. Supplemental Video 6 shows this the evolution of this tracer from 2004 through the

401   end of 2013.

402   4. Discussion

403   We describe a 10+ year long, high-resolution simulation which achieves 1/60° horizontal

404   resolution in the Labrador Sea via two nests inside a regional configuration, resolving mesoscale

405   and sub-mesoscale processes which strongly impact the deep convection which occurs here.

406   We show that lower-resolution simulations fail to resolve these key processes that strongly

407   control the production of Labrador Sea Water, an important water mass within the Atlantic

408   Meridional Overturning Circulation. While the NATL60 and eNATL60 simulations were designed

409   with the SWOT altimetry satellite mission in mind (NATL60 website: https://meom-

410   group.github.io/swot-natl60/virtual-ocean.html), their integration period, like many other high-

411   resolution simulations, is a handful of years. LAB60, although covering a much smaller region,

412   could be a valuable asset to many users who require a lengthy period of high-resolution model

413   output. We also have included three passive tracers which are often excluded in simulations at

414   this resolution. Our three passive tracers highlight regions where each water mass enters the

415   interior region of the Labrador Sea, demonstrating the pathways of buoyant Greenland melt

416   and Irminger water. Furthermore, we trace Labrador Sea Water which is formed during the

417   convective winter period.

418   We show that LAB60 has greater EKE than our lower-resolution simulation, resolving

419   eddy fluxes including Irminger Rings, boundary current eddies, and likely convective eddies as

420   indicated by greater EKE within the interior. Boundary current eddies still appear relatively

421   disconnected from the interior basin, adding further support that these eddies have limited

422   influence on convection and restratification (Rieck et al., 2019). We offer no additional support

423   regarding the relative importance of Irminger Rings and convective eddies on controlling deep

424   convection; this is currently being investigated for a later manuscript. Model drift appears very

425   low, a large improvement over the ANHA4 and ANHA12 configurations. The drift might produce

426   slightly denser LSW than observations suggest, however LAB60s density is much more accurate

427 than ANHA4 and ANHA12. The boundaries of LAB60, supplied by the inner SPG12 nest, may

428 influence the high-resolution nest. We note that the North Atlantic Current, which is close to

429 the boundary, has less EKE and vorticity than the ANHA4 and ANHA12 simulations. Conversely,

430 the WGC close to the eastern nested boundary has multiple jets which have been noted in

431 hydrographic data (Pickart, personal communication). Boundary communication is always a

432 concern in nested simulations and LAB60 is no different. More investigation will reveal any

433 potential boundary issues but our results so far indicate no further areas of potential concern.

434   Others have investigated the Labrador Sea using numerical simulations with different

435 resolution. Böning et al. (2016) traced Greenland meltwater with the 1/20° VIKING20 and 1/4°

436 ORCA025 simulations, noting more meltwater entered the interior Labrador Sea at higher

437 resolution partially as a result of greater WGC eddy fluxes but not from the Labrador coast. The

438 minor amount of eddy fluxes from the Labrador coast has been noted earlier even at lower

439 resolution (1/3°; Myers, 2005). Steadily increasing horizontal resolution has so far not changed

440 this for the Labrador coast, though this is opposite for the WGC. LAB60 has a clear increase in

441 EKE and likely greater eddy fluxes from the WGC into the interior of the Labrador Sea.

442   We have many ambitious research topics which we plan to use LAB60 to investigate.

443 This includes, but is not limited to, the variability and structure of the West Greenland Coastal

444 Current, Labrador Sea Water production, and the role of both Irminger Rings and convective

445 eddies in controlling stratification in the Labrador Sea. This lengthy high-resolution simulation

446 with three passive tracers will provide valuable information for many numerical studies within

447 the Labrador Sea for years to come.

448

449 Code and/or data availability

450   The FORTRAN code used to carry out the LAB60 simulation can be accessed from the

451 NEMO version 3.6 repository

452 (https://forge.ipsl.jussieu.fr/nemo/browser/NEMO/releases/release-3.6). A few FORTRAN files

453 were modified to handle our passive tracers. The complete FORTRAN files as well as the

454 CPP.keys, namelists, and associated files can be found on Zenodo (Pennelly, 2020). Initial and

455 boundary conditions, atmospheric forcing, and numerical output were too large to host on a

456 repository and instead are hosted on our lab's servers as well as the Compute Canada Niagara

457 server. These data can be requested by emailing the corresponding author.

458

459 Author Contribution

460   PM designed the layout of the LAB60 configuration which included the region of

461 interest, numerical length, and which forcing and initial conditions to supply, as well as

462 supervised CP. CP produced the configuration, modified the FORTRAN code, set up the

463 configuration on the high-performance computing systems, carried out the simulation, and

464 performed the analysis. The manuscript was prepared by CP with contributions by PM.

465

466 Acknowledgements

475

476 The authors declare that they have no conflict of interest.

477

478

479 References

480 Amante, C. and Eakins, B.W.: ETOPO1 1 Arc-minute global relief model: procedures data

481 sources and analysis. NOAA Technical Memorandum NESDIS, NGDC-24 19, 2009.

482 Bacon, S., Gould, W.J., and Jia, Y.: Open-ocean convection in the Irminger Sea. Geophysical

483 Research Letters, 30(5), 2003.

484   Bamber, J., van den Broeke, M., Ettema, J., Lenaerts, J., and Rignot, E.: Recent large increases in

485   freshwater fluxes from Greenland into the North Atlantic. Geophysical Research Letters, 39(19),

486   2012.

487   Barnier, B., Madec, G., Penduff, T., Molines, J-M., Treguier, A-M., Le Sommer, J., Beckmann, A.,

488   Biastoch, A., Böning, C., Dengg, J., Derval, C., Durand, E., Gulev, S., Remy, R., Talandier, C.,

489   Theetten, S., Maltrud, M., Mcclean, J., and De Cuevas, B.: Impact of partial steps and

490   momentum advection schemes in a global ocean circulation model at eddy permitting

491   resolution. Ocean Dynamics, 56 (5-6), 543-567, 2006.

492   Böning, C.W., Behrens, E., Biastoch, A., Getzlaff, K., and Bamber, J.L.: Emerging impact of

493   Greenland meltwater on deepwater formation in the North Atlantic Ocean. Nature Geoscience,

494   97(7), 523, 2016.

495   Brossier, C.L., Léger, L., Giordani, H.,Beuvier, J., Bouin, M.N., Ducrocq, W., and Fourrié, N.:

496   Dense water formation in the north-western Mediterranean area during HyMeX-SOP2 in 1/36°

497   ocean simulations: Ocean-atmosphere coupling impact. Journal of Geophysical Research:

498   Oceans, 122(7), 5749-5773, 2017.

499   Bryden, H.L., Longworth, H.R., and Cunningham, S.A.: Slowing of the Atlantic meridional

500   overturning circulation at 25°N. Nature, 438(7068), 655, 2005.

501   Cael, B.B. and Jansen, M.F.: On freshwater fluxes and the Atlantic meridional overturning

502   circulation. Limnology and Oceanography, 5(2), 185-192, 2020.

503   Chanut, J., Barnier, B., Large, W., Debreu, L., Penduff, T., Molines, J.M., and Mathiot, P.:

504   Mesoscale eddies in the Labrador Sea and their contribution to convection and restratification.

505   Journal of Physical Oceanography, 28(8), 1617-1643, 2008.

506   Chassignet, E.P. and Xu, X.: Impact of horizontal resolution (1/12 to 1/50) on Gulf Stream

507   separation, penetration, and variability. Journal of Physical Oceanography, 47(8), 1999-2021,

508   2017.

509   Courtois, P., Hu, X., Pennelly, C., Spence, P., and Myers, P.G.: Mixed layer depth calculation in

510   deep convection regions in ocean numerical models. Ocean Modelling, 120, 60-78, 2017.

511   Cuny, J., Rhines, P.B., and Kwok, R.,: Davis Strait volume, freshwater and heat fluxes. Deep Sea

512   Research Part I: Oceanographic Research Papers, 52.3, 519-542, 2005.

513   Curry, B., Lee, C.M., and Petrie, B.: Volume, freshwater, and heat fluxes through Davis Strait,

514   2004-05. Journal of Physical Oceanography, 41(3), 429-436, 2011.

515   Curry, B., Lee, C.M., Petrie, B., Moritz, R.E. and Kwok, R.: Multiyear volume, liquid freshwater,

516   and sea ice transports through Davis Strait, 2004-10. Journal of Physical Oceanography, 44(4),

517   1244-1266, 2014.

518   Dai, A., Qian, T., Trenberth, K.E., and Milliman, J.D.: Changes in continental freshwater

519   discharge from 1948 to 2004. Journal of Climate, 22(10), 2773-2792, 2009.

520   Debreu, L., Vouland, C., and Blayo, E.: AGRIF: Adaptive grid refinement in Fortran. Computers

521   and Geosciences, 34(1), 8-13, 2008.

522   Dussin, R., Barnier, B., and Brodeau, L.: The making of Drakkar forcing set DFS5, Grenoble,

523   France: LGGE, 2016.

524   Ferry, N., Parent, L., Garric, G., Barnier, B., and Jourdain, N.C.: Mercator global eddy permitting

525   ocean reanalysis GLORYS1V1: Description and results. Mercator-Ocean Quarterly Newsletter,

526   36, 15-27, 2010.

527   Fichefet, T., and Maqueda, M.A.M.: Sensitivity of a global sea ice model to the treatment of ice

528   thermodynamics and dynamics. Journal of Geophysical Research: Oceans, 102(C6), 12609-

529   12646, 1997.

530   Fischer, J., Visbek, M., Zantopp, R., Nunes, N.: Interannual to decadal variability of outflow from

531   the Labrador Sea. Geophysical Research Letters, 37(24), 2010.

532   Frajka-Williams, E., Rhines, P.B., and Eriksen, C.C.: Horizontal stratification during deep

533   convection in the Labrador Sea. Journal of Physical Oceanography, 44(1), 220-228, 2014.

534   Fratantoni, P.S. and Pickart, R.S.: The Western North Atlantic Shelfbreak Current System in

535   Summer. Journal of Physical Oceanography, 37(10), 2509-2533, 2007.

536   Fresnay, S., Ponte, A.L., Le Gentil, S., Le Sommer, J.: Reconstruction of the 3-D dynamics from

537   surface variable in a high-resolution simulation of the North Atlantic. Journal of Geophysical

538   Research: Oceans, 123(3), 1612-1630, 2018.

539   Garcia-Quintana, Y., Courtois, P., Hu, X., Pennelly, C., Kieke, D., and Myers, P.G.: Sensitivity of

540   Labrador Sea Water formation to changes in model resolution, atmospheric forcing, and

541   freshwater input. Journal of Geophysical Research: Oceans, 124(3), 2126-2152, 2019.

542 Gelderloos, R., Katsman, C.A. and Drijfhout, S.S.: Assessing the roles of three eddy types in

543 restratifying the Labrador Sea after deep convection. Journal of Physical Oceanography, 41(11),

544 2102-2119, 2011.

545 Gordon, A.L., Visbeck, M., and Comiso, J.C.: A possible link between the Weddell Polynya and

546 the Southern Annular Mode. Journal of Climate, 20(11), 2558-2571, 2007.

547 Hansen, B., and Østerhus, S.: North Atlantic-Nordic Seas exchanges. Progress in Oceanography,

548 45(2), 109-208, 2000.

549 Hátún, H., Eriksen, C.C., and Rhines, P.B.: Buoyant eddies entering the Labrador Sea observed

550 with gliders and altimetry. Journal of Physical Oceanography, 37(12), 2838-2854, 2007.

551 Holte, J., and Talley, L.: A new algorithm for finding mixed layer depths with applications to

552 Argo data and Subantarctic Mode Water formation. Journal of Atmospheric and Oceanic

553 Technology, 26(9), 1920-1939, 2009.

554 Kieke, D., Klein, B., Stramma, L., Rhein, M., and Koltermann, K.P.: Variability and propagation of

555 Labrador Sea Water in the southern subpolar North Atlantic. Deep Sea Research Part I:

556 Oceanographic Research Papers, 56(10), 1656-1674, 2009.

557 Lab Sea Group: The Labrador Sea deep convection experiment. Bulletin of the American

558 Meteorological Society, 79(10), 2033-2058, 1998.

559 Large, W.G., and Yeager, S.G.: The global climatology of an interannually varying air-sea flux

560 data set. Climate Dynamics, 33(2-3), 341-364, 2008

561 Latif, M., Roechner, E., Mikolajewicz, U., and Voss, R.: Tropical stabilization of the thermohaline

562 circulation in a greenhouse warming simulation. Journal of Climate, 13(11), 1809-1813, 2000.

563 Lazier, J., Hendry, R., Clarke, A., Yashayaev, I., and Rhines, P.: Convection and restratification in

564 the Labrador Sea, 1990-2000. Deep Sea Research Part I: Oceanographic Research Papers,

565 49(10), 1819-1835, 2002.

566 Lazier, J.R.N., and Wright, D.G.: Annual velocity variations in the Labrador Current, Journal of

567 Physical Oceanography, 23(4), 659-678, 1993.

568 Lilly, J.M., Rhines, P.B., Visbeck, M., Davis, R., Lazier, J.R.N., Schott, F., and Farmer, D.: Observing

569 deep convection in the Labrador Sea during winter 1994/95. Journal of Physical Oceanography,

570 29, 2065-2098, 1999.

Lilly, J.M., Rhines, P.B., Schott, F., Lavender, K., Lazier, J., Send, U., and D'Asaro, E.: Observations of the Labrador Sea eddy field. Progress in Oceanography, 59(1), 75-176, 2003.

Lin, P., Pickart, R.S., Torres, D.J., and Pacini, A.: Evolution of the freshwater coastal current at the southern tip of Greenland. Journal of Physical Oceanography, 48(9), 2127-2140. 2018

Madec, G.: Note du Pôle de modélisation. Institut Pierre-Simon Laplace (IPSL), France, No 27, ISSN No 1288-1619, 2008.

Marshall, J. and Schott, F.: Open-ocean convection: Observations, theory, and models. Reviews of Geophysics, 37(1), 1-64, 1999.

Marzocchi, A., Hurshi, J.J.M., Holiday, N.P., Cunningham, S.A., Blaker, A.T., and Coward, A.C.: The North Atlantic subpolar circulation in an eddy-resolving global ocean model. Journal of Marine Systems, 142, 126-143, 2015.

McGeehan, I. and Maslowski, W.: Impact of shelf-basin freshwater transport on deep convection in the western Labrador Sea. Journal of Physical Oceanography, 41(11), 2187-2210, 2011.

Müller, V., Kieke, D., Myers, P.G., Pennelly, C., and Mertens, C.: Temperature flux carried by individual eddies across 47° in the Atlantic Ocean. Journal of Geophysical Research: Oceans, 122(3), 2441-2464, 2017.

Müller, V., Kieke, D., Myers, P.G., Pennelly, C., Steinfeldt, R., and Stendardo, I.: Heat and freshwater transport by mesoscale eddies in the southern subpolar North Atlantic. Journal of Geophysical Research: Oceans, 124(8), 5565-5585, 2019.

Myers, P.: Impact of freshwater from the Canadian Arctic Archipelago on Labrador Sea water formation. Geophysical Research Letters, 32(6), 2005.

Pennelly, C.: A 1/60 degree NEMO configuration within the Labrador Sea: LAB60, Zenodo, http://doi.org/10.5281/zenodo.3762748, 2020.

Pennelly, C. Hu, X., and Myers, P.G.: Cross-isobath freshwater exchange within the North Atlantic Subpolar Gyre. Journal of Geophysical Research: Oceans, 124(10), 6831-6853, 2019.

Rattan, S., Myers, P.G., Treguier, A.M., Theetten, S., Biastoch, A., and Böning, C. Towards an understanding of Labrador Sea salinity drift in eddy-permitting simulations. Ocean Modelling, 35(102), 77-88, 2010.

600 Rieck, J.K., Böning, C.W., and Getzlaff, K.: The nature of eddy kinetic energy in the Labrador Sea:

601 Different types of mesoscale eddies, their temporal variability, and impact on deep convection.

602 Journal of Physical Oceanography, 49(8), 2075-2094, 2019.

603 Schmidt, S. and Send, U.: Origin and composition of seasonal Labrador Sea freshwater. Journal

604 of Physical Oceanography, 37(6), 1445-1454, 2007.

605 Schulze, L.M., Pickart, R.S., and Moore, G.W.K.: Atmospheric forcing during active convection in

606 the Labrador Sea and its impact on mixed-layer-depths. Journal of Geophysical Research:

607 Oceans, 121(9), 6978-6992, 2016.

608 Smith, G.C., Roy, F., Mann, P., Dupont, F., Brasnett, B., Lemieux, J.F., Laroche, S., and Bélair, S.:

609 A new atmospheric dataset for forcing ice-ocean models: Evaluation of reforecasts using the

610 Canadian global deterministic prediction system. Quarterly Journal of the Royal Meteorological

611 Society, 140(680), 881-894, 2014.

612 Straneo, F.: Heat and freshwater transport through the central Labrador Sea. Journal of Physical

613 Oceanography, 36(4), 606-628, 2006.

614 Straneo, F. and Saucier, F.: The arctic-subarctic exchange through Hudson Strait. Arctic-

615 Subarctic Ocean Fluxes, Springer, Dordrecht, 249-261, 2008.

616 De Steur, L., Hansen, E., Gerdes, R., Karcher, M., Fahrbach, E., Holfort, J.: Freshwater fluxes in

617 the East Greenland Current: A decade of observations. Geophysical Research Letters, 36(23),

618 2009.

619 Su, Z., Wang, J., Klein, P., Thompson, A.F., and Menemenlis, D.: Ocean submesoscales as a key

620 component of the global heat budget. Nature communications, 9(1), 1-8, 2018.

621 Tréquier, A.M., Theetten, S., Chassignet, E.P., Penduff, T., Smith, R., Talley, L., Beismann, J.O.,

622 and Böning, C.: The North Atlantic subpolar gyre in four high-resolution models. Journal of

623 Physical Oceanography, 35(5), 757-774, 2005.

624 Yashayaev, I. and Loder, J.W.: Recurrent replenishment of Labrador Sea Water and associated

625 decadal-scale variability. Journal of Geophysical Research: Oceans, 121(11), 8095-8814, 2016.

626 Yashayaev, I.: Hydrographic changes in the Labrador Sea, 1960-2005. Progress in

627 Oceanography, 73(3-4), 242-276, 2007.

628 Whiteworth, T. and Orsi, A.H.: Antarctic Bottom Water production and export by tides in the

629 Ross Sea. Geophysical Research Letters 33(12), 2006.

630 Zalesak, S.T.: Fully multidimensional flux-corrected transport algorithms for fluids. Journal of

631 computational physics, 31(3), 335-362, 1979.

632

633 Tables

634

635 Table 1: Domain settings for the ANHA4 parent domain, SPG12 and LAB60 nested domains.

636 Other settings which are invariant to the domain are shown in Table 2.

Setting	ANHA4	SPG12	LAB60
Horz. Resolution	1/4°	1/12°	1/60°
X points	544	724	1179
Y points	800	694	2659
Timestep [s]	720	240	48
Horiz. Eddy Viscosity [$m^4 s^{-1}$]	1.5x10^11	1.5x10^10	3.5x10^8
Horiz. Eddy Diffusivity [$m^2 s^{-1}$]	300	50	20
Lateral Slip Conditions	Free slip	Free slip	No slip

637

638

639

640

641

642

643

644

645

646

647

648

649

650   Table 2: Model configuration settings which are identical between all three domains. **Bold**

651   values indicate values which were changed when we migrated LAB60 from the Graham cluster

652   to Niagara.

Configuration Setting	Value
Vertical grid	75 geopotential levels
Sea-ice model	LIM 2 (Fichefet and Maqueda, 1997)
Bulk formula	CORE (Large and Yeager, 2008)
Liquid discharge	Dia et al. (2009) + Bamber (2012: Greenland)
Solid discharge	Input as liquid
Surface Restoring	None
Initial conditions	Glorys1v1 (T,S,U,V,SSH,ice)
Open boundary conditions	Glorys1v1 (T,S,U,V,ice)
Atmospheric forcing:	
2002-2006	CGRF (Smith et al, 2014)
2007-2017	Drakkar Forcing Set 5.2 (Dussin et al. 2016)
Lateral momentum	Bilaplacian operator
Lateral diffusion	Laplacian operator
Vertical eddy viscosity	$1\times10^{-4}\,m^2\,s^{-1}$
Vertical eddy diffusivity	$1\times10^{-5}\,m^2\,s^{-1}$
Mixed layer scheme	Holte and Talley (2009)
Bottom friction	Nonlinear
Hydrostatic approximation	Yes
Passive tracers	Three (see Figure 2)
CPU requested	672 (**3000**), Broadwell 2.1 GHz (Skylake 2.4 GHz)
Time to complete 1 year	Approximately 700 (**200**) hours
Initialization date	January 1st, 2002

653

654

655   Figures
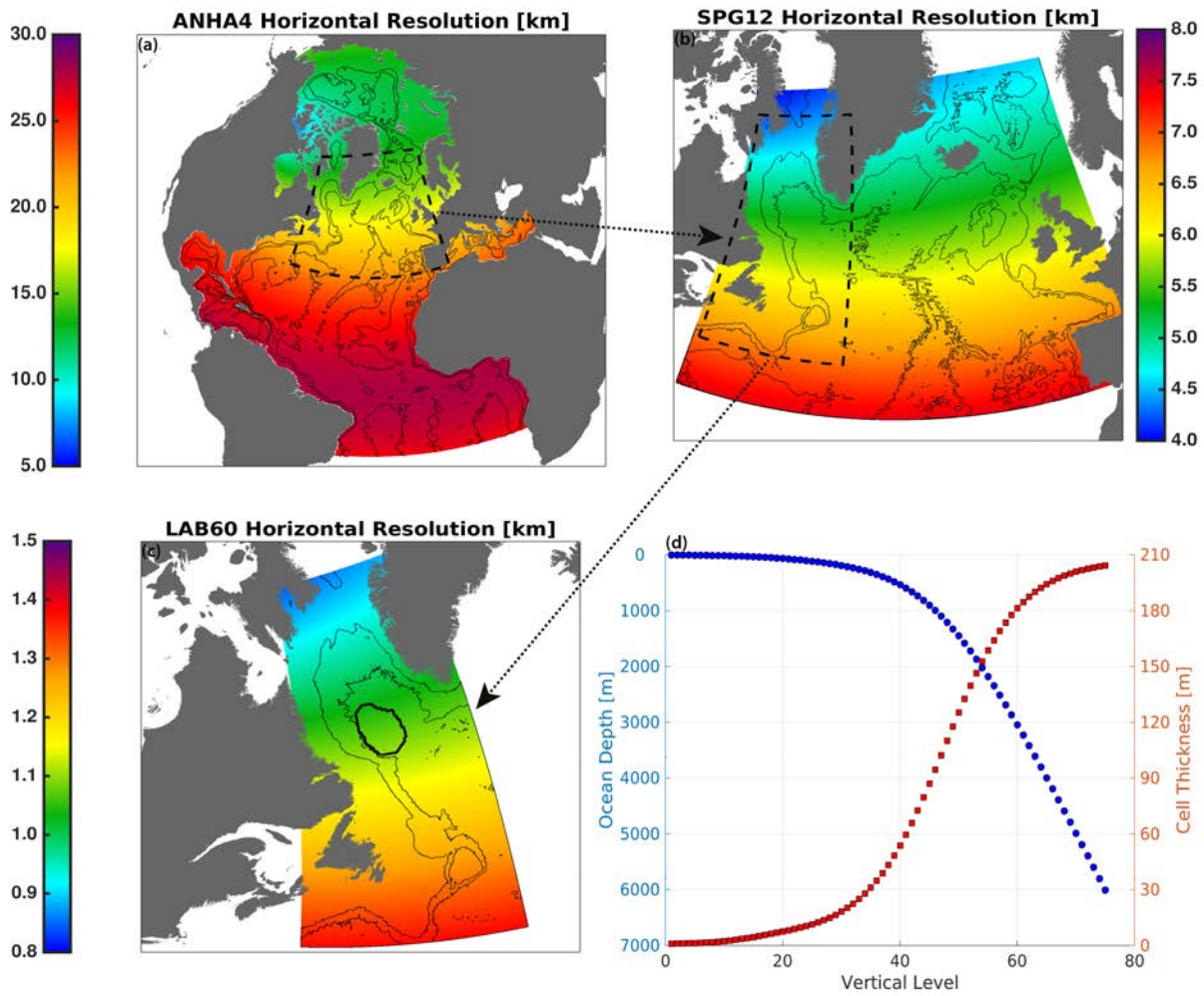
Figure 1: Domain setup for the (a) ANHA4 parent domain, (b) the SPG12 nest, and (c) the LAB60 nest. Horizontal grid resolution, in km, is identified by color. All domains share identical vertical grid structure (d). The thick black contour in (c) identifies a region of interest where calculations of LSW's density, thickness, and mixed layer depth are determined. The 1000m, 3000m, and 5000m isobaths are shown via the thin black contours.
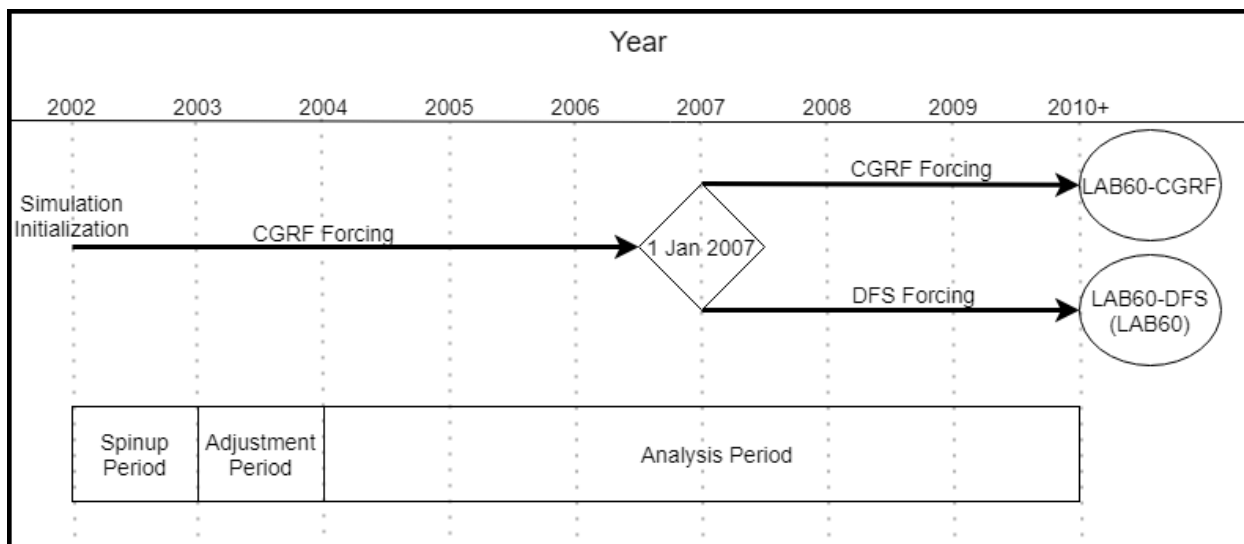
Figure 2: Diagram showing the multiple periods of the LAB60 simulation. The original simulation was initialized with CGRF atmospheric forcing in 2002, although a branch swapping to DFS occurred at the start of 2007. This DFS branch is what is primarily presented in this study.
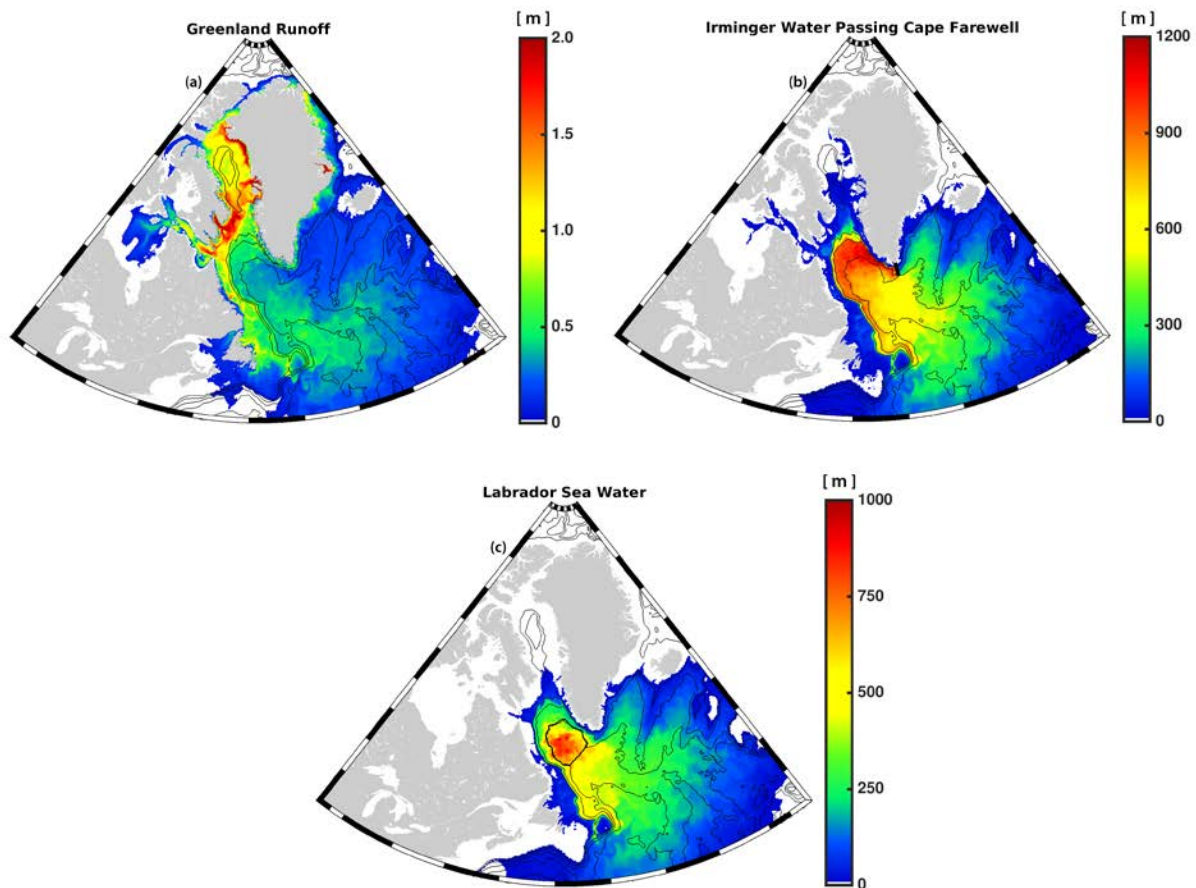
669

670   Figure 3: The three passive tracers used within our LAB60 simulation with source regions

671   indicated by thick black lines: (a) Greenland runoff, (b) Irminger Water (T > 3.5°C, S > 34.88)

672   which flows west past Cape Farwell, and (c) Labrador Sea Water (σ_θ>27.68 kg m^{-3}) produced

673   each convective season. Images are from the simulation date 1 Jan 2010. Bathymetric contours

674   are every 1000m. Units are the thickness, in meters, of the tracer. Note: as all three domains

675   are included in this figure, spatial resolution changes within each subfigure.
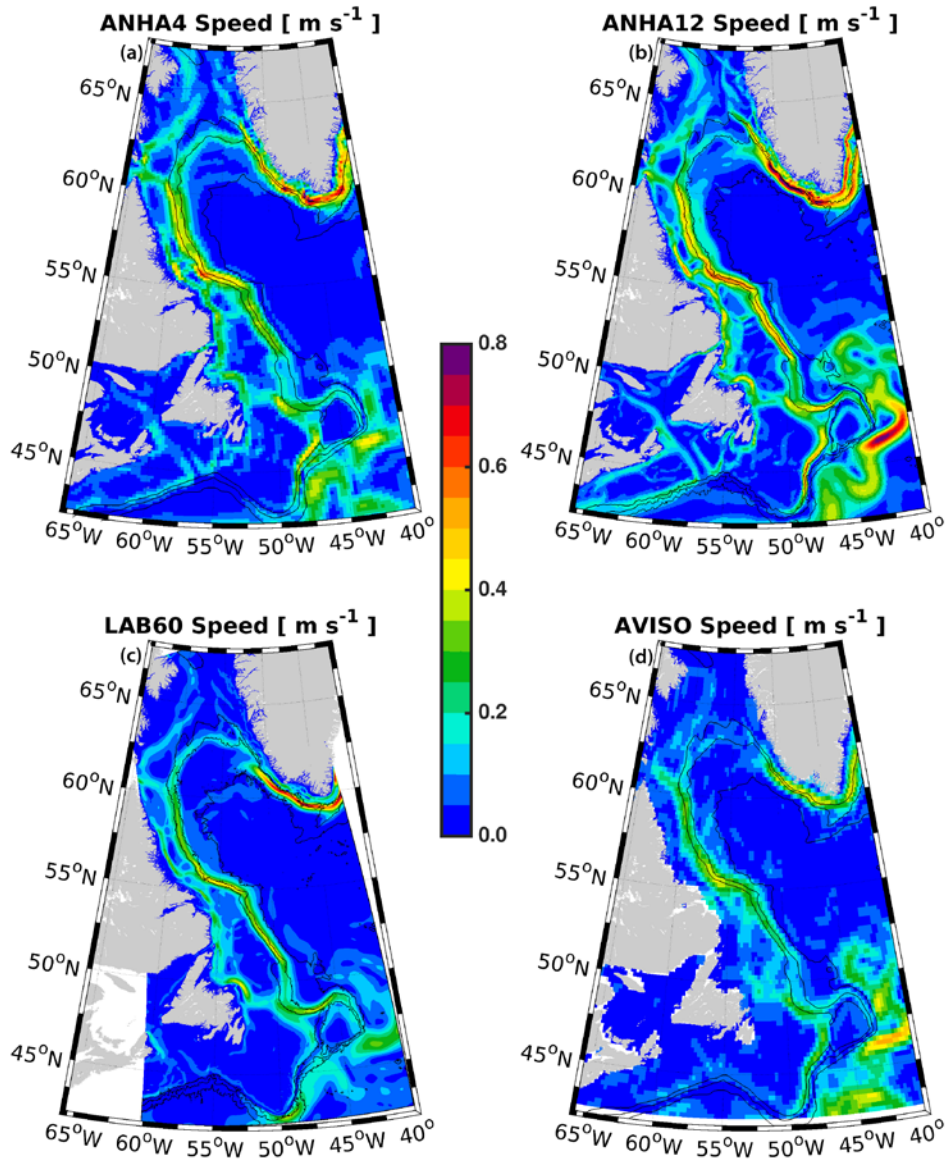
Figure 4: Top 50m average speed (2004-2013) for the (a) ANHA4, (b) ANHA12, (c) and LAB60 simulations, as well as (d) from AVISO observations. The 1000, 2000, and 3000m isobaths are shown by the black contour lines.
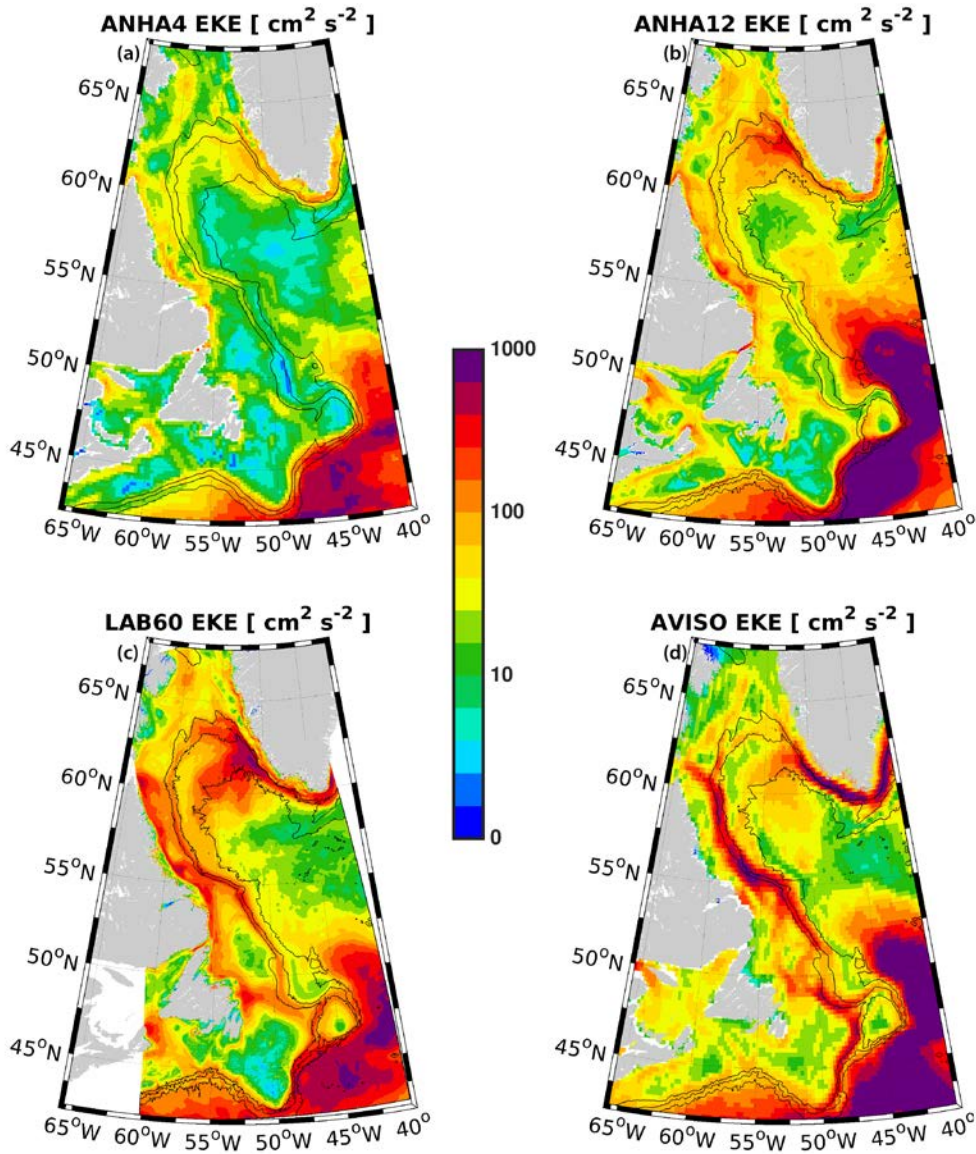
Figure 5: Eddy kinetic energy (EKE), as calculated from geostrophic velocities resulting from the sea level height anomaly, are shown for (a) ANHA4, (b) ANHA12, and (c) our LAB60 simulation, from 2004 to 2013. Observations via AVISO are identified in (d). The 1000m, 2000m, and 3000m isobaths are shown by the black contour lines. A log scale was used for clarity.
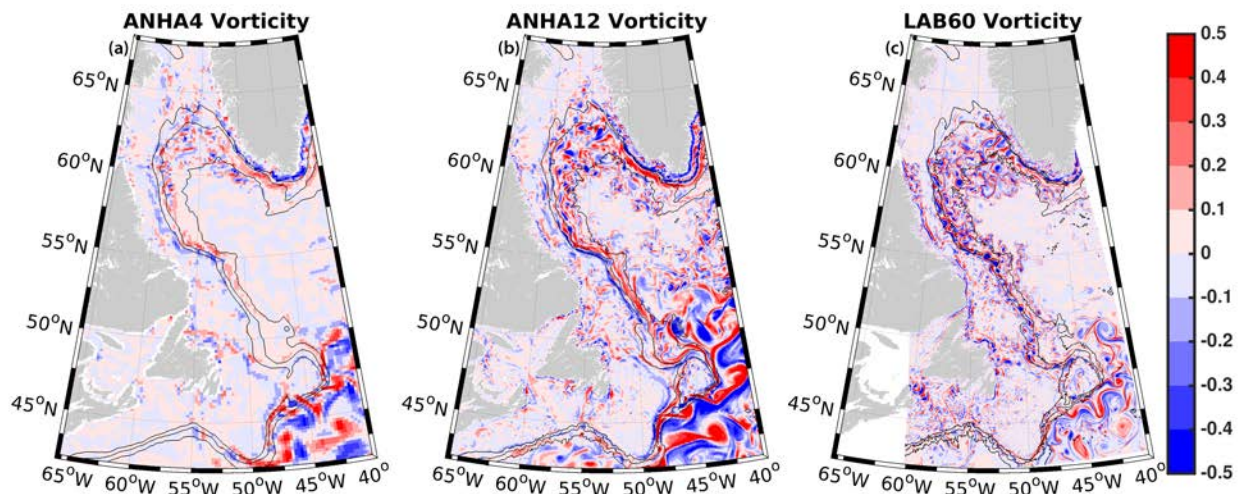
Figure 6: Top 50m relative vorticity, normalized by the planetary vorticity, as simulated by (a) ANHA4, (b) ANHA12, and (c) LAB60 on 16 March 2008. The 1000m, 2000m, and 3000m isobaths are shown by the black contour lines.
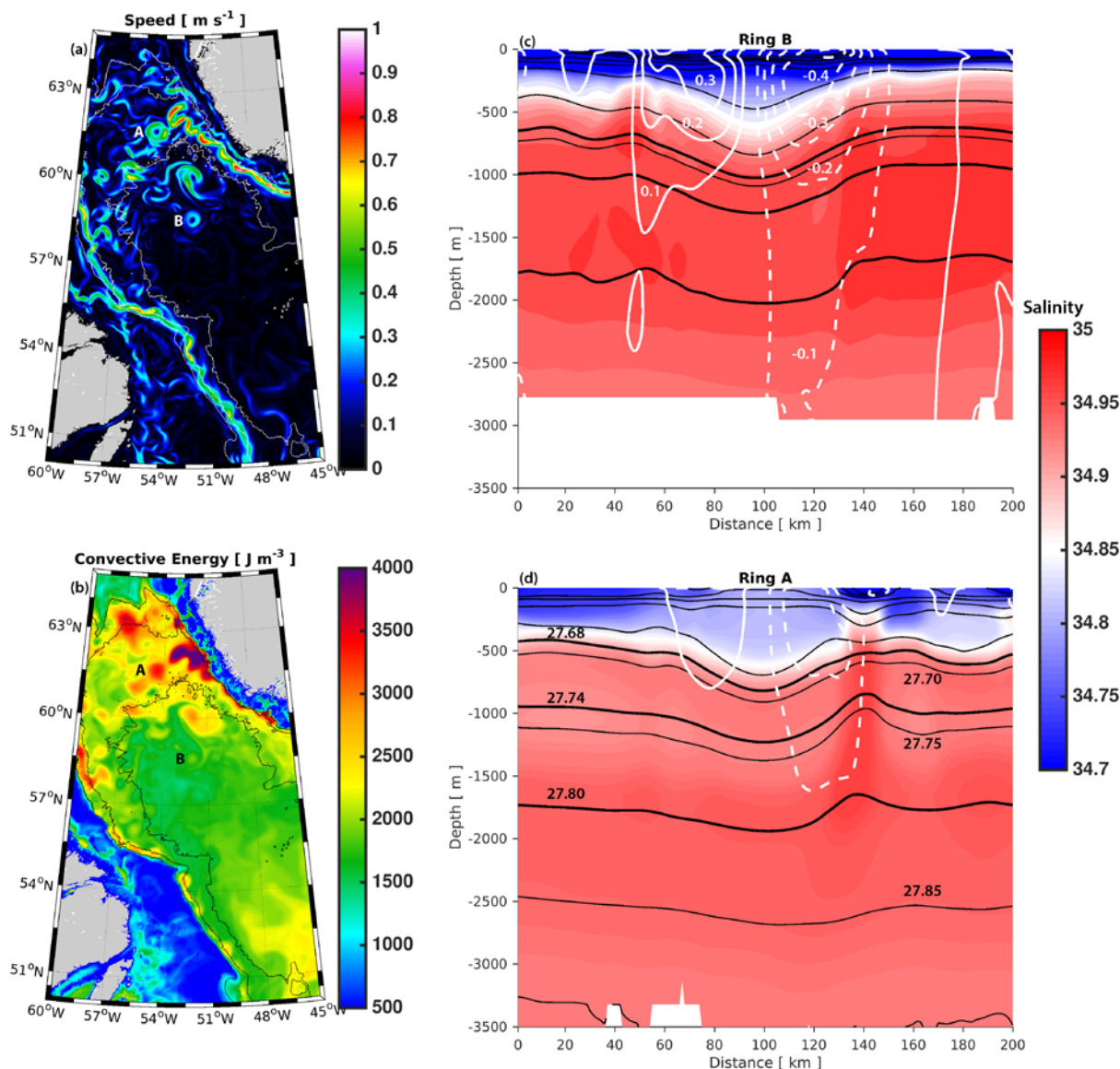
Figure 7: LAB60 snapshot (26 July 2007) of the surface speed (a) and convective energy (b) within the Labrador Sea. Two Irminger Rings are identified by their age with letters: Ring A is a young Irminger Ring, while Ring B is comparatively older. An east-west cross section through each of these Irminger Rings is shown in (c) and (d) where colors indicate salinity, black contours indicate potential density using a contour interval of 0.05 kg m^{-3}, and white contours indicate meridional velocity where southern flow is dashed and northern flow is solid, using a contour interval of 0.1 m s^{-1}. Thick black contours indicate the potential density classification of Upper Labrador Sea Water (σ_θ=27.68 to 27.74 kg m^{-3}) and Classical Labrador Sea Water (σ_θ= 27.74 to 27.80 kg m^{-3}).
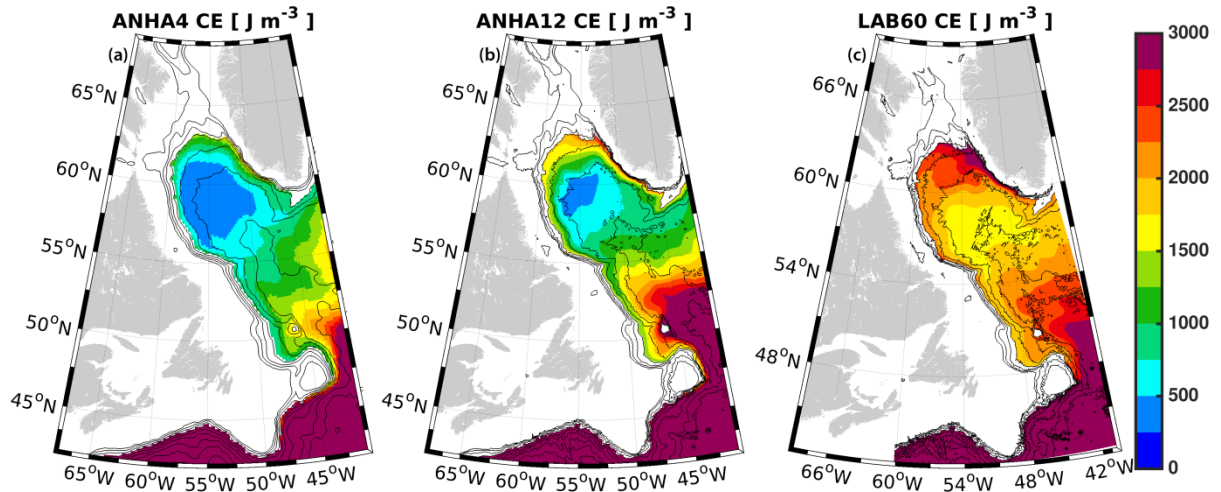
Figure 8: Convective energy (CE), the strength of stratification down to a reference depth of 2000m, is shown for (a) ANHA4, (b) ANHA12, and (c) LAB60. Convective energy was averaged from 2004 through 2013. Values where the depth of the seafloor was less than 2000m were removed to preserve clarity. Bathymetric contours (black lines) are shown every 500m.

712
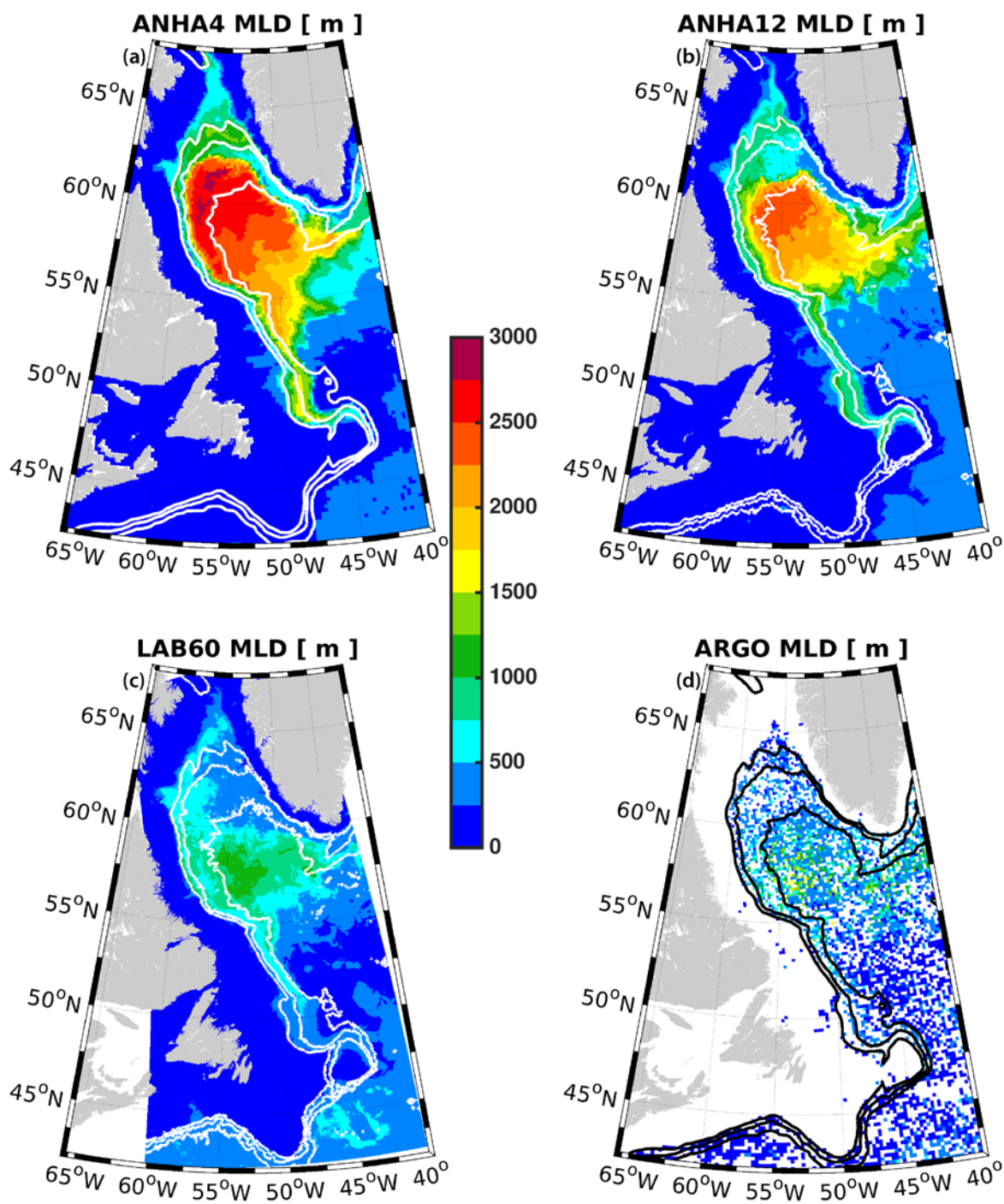
Figure 9: Maximum mixed layer depth for (a) ANHA4, (b) ANHA12, (c) LAB60, as well as (d)

ARGO observations, where available, from 2004 through the end of 2013. For clarity, the ARGO

data were placed on the same grid as ANHA4. The 1000m, 2000m, and 3000m isobaths are

shown via the white and black contours

717
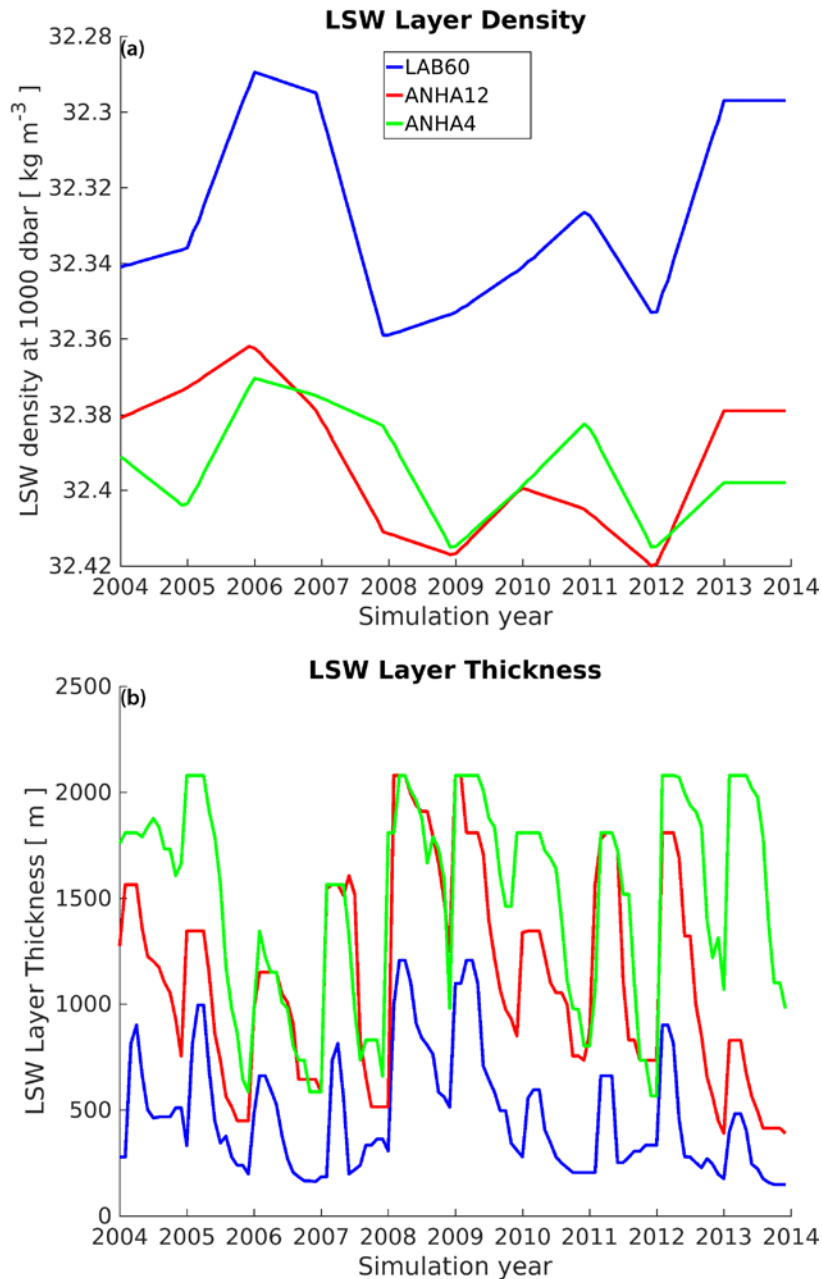
718

719 Figure 10: Labrador Sea Water (LSW) density (a) and thickness (b) for the LAB60, ANHA12, and

720 ANHA4 configurations. LSW density was determined from the thickest layer where a 0.001 kg

721 m^{-3} change in potential density (ref: 1000 dbar) occurred within the black polygon outlines in

722 Fig 1c. The LSW layer was then calculated between this density and one which was 0.02 kg m^{-3}
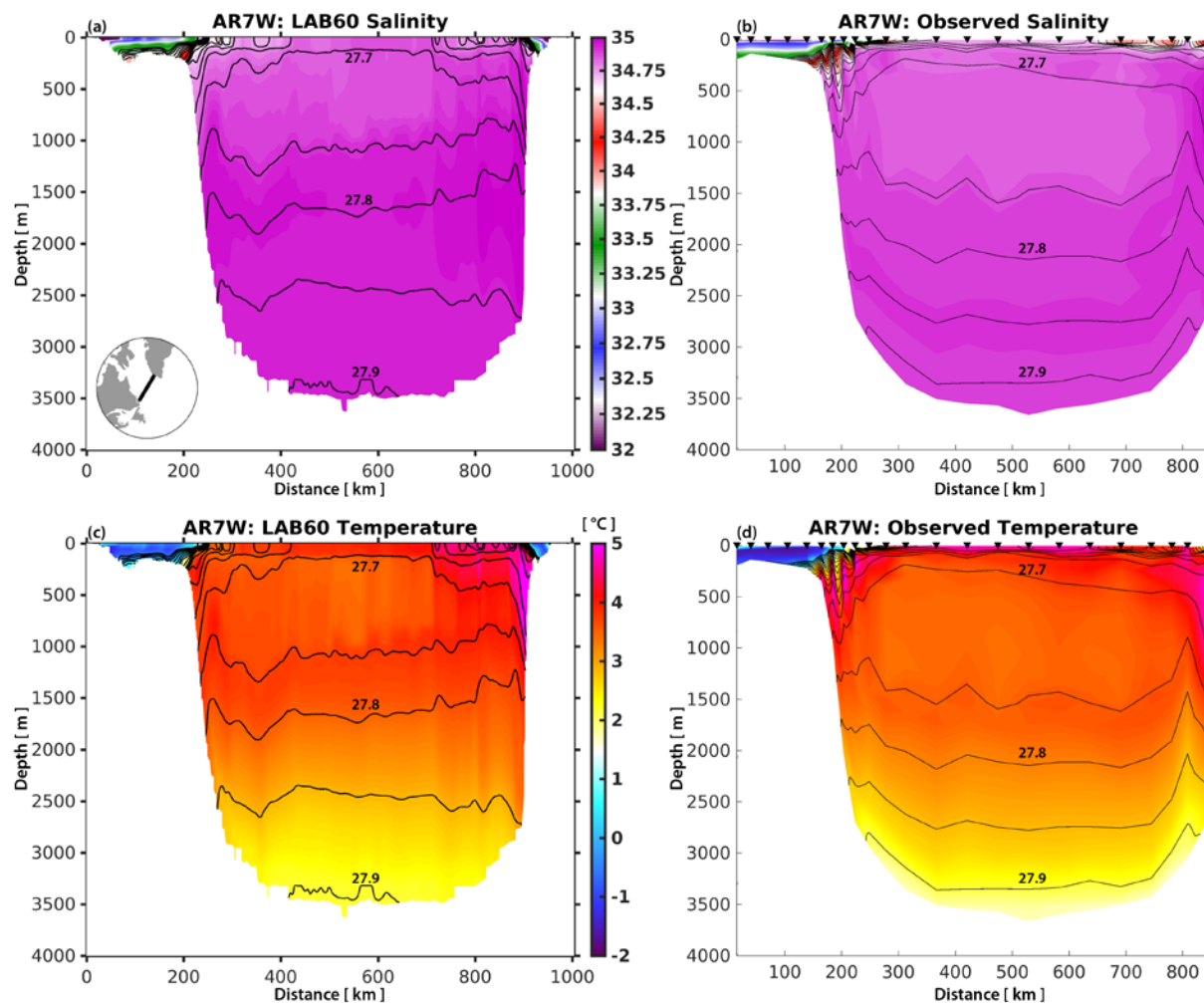
723 less dense.

724
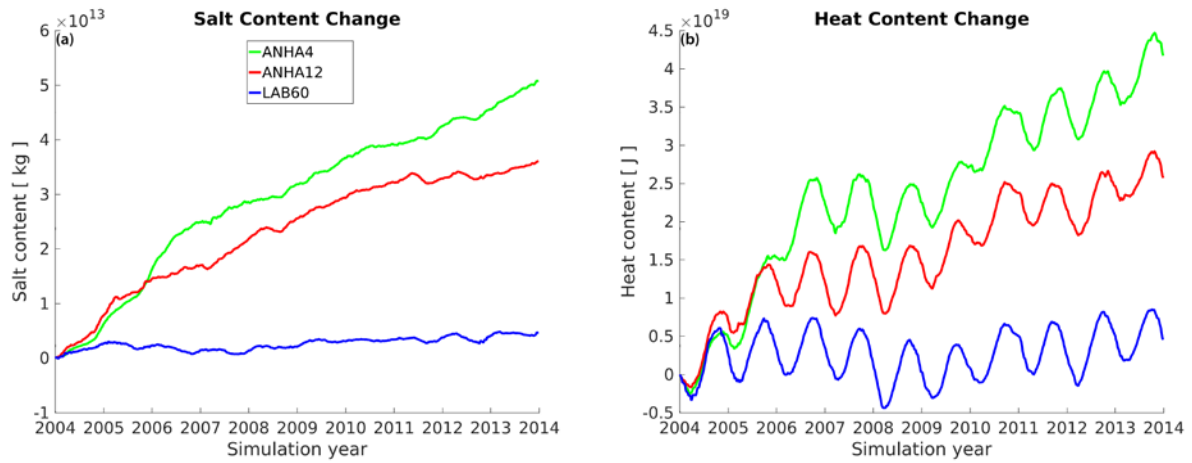
Figure 11: Numerical salt (a) and heat (b) drift in our three simulations as they evolve since 1 Jan 2004. Salt and heat content is calculated over the full ocean column within the polygon in Fig. 1c.

730

Figure 12: Salinity (top) and temperature (bottom) section across AR7W as determined by the
LAB60 simulation (left) and observations (right) from May 2008. Downward triangles identify
collection sites across the AR7W transit carried out by the CCGS Hudson. Potential density
(black contours) isopycnal interval is 0.05 kg m^{-3}.